Materials Advances

ROYAL SOCIETY OF CHEMISTRY

PAPER

View Article Online
View Journal | View Issue

Cite this: *Mater. Adv.*, 2026, 7, 649

Comparative assessment of FTO and ITO substrates for $BiVO_4$ photoanodes: superior surface quality enabling faster water oxidation in ITO

Yeon Gyo Shim,[ab] Yuki Nakatsukasa,[c] Kana Matsumoto,[c] Ji Eun Kim,[a] Su Jin Kim,[a] Seung Heon Choi,[ab] Seung Hyeon Jeong,[ab] Seong Kyu Jang,[ab] Aram Hong,[b] Kenji Katayama[c] and Woon Yong Sohn*[ab]

We fabricated bismuth vanadate ($BiVO_4$) photoanodes using the metal–organic decomposition (MOD) method on fluorine-doped tin oxide (FTO) and indium tin oxide (ITO) substrates to compare their photoelectrochemical (PEC) performance. The current density of FTO/$BiVO_4$ (F/B, 0.671 mA cm^{-2} at 1.23 V_{RHE}) was higher than that of ITO/$BiVO_4$ (I/B, 0.210 mA cm^{-2} at 1.23 V_{RHE}). Although the surface quality of $BiVO_4$ appeared to be better when grown on ITO, the poor junction between ITO and $BiVO_4$ was identified as the primary cause of the low current density, as evidenced by the lower charge separation efficiency and higher resistance observed in the I/B (F/B: 112.1 Ω, I/B: 249.3 Ω). Pattern-illumination time-resolved phase microscopy (PI–PM) further revealed that more electrons remained on the I/B surface due to inefficient electron transfer to the ITO substrate. In addition, rapid trap-mediated recombination in the I/B, as confirmed by near-field heterodyne transient grating (NF-HD-TG) analysis, further supports these findings and likely contributes to the low current density. However, it was observed that water oxidation occurred more rapidly on I/B (τ = 0.281 s) compared to F/B (τ = 0.553 s), which appears to be due to the superior surface quality. This suggests that if substrate damage from heat can be minimized, ITO may be more suitable than FTO for photoelectrodes for water oxidation.

Received 7th October 2025,
Accepted 23rd November 2025

DOI: 10.1039/d5ma01153a

rsc.li/materials-advances

1. Introduction

Transparent conducting oxides (TCOs) are essential components of many optoelectronic systems, such as photoelectrochemical (PEC) cells, solar cells, and LEDs, because they combine high optical transparency with electrical conductivity.[1–4] TCOs serve as substrates for photoelectrodes by providing strong interfacial adhesion to mechanically support the photoactive semiconductor layer and by ensuring efficient charge transfer to the external circuit through good electrical contact. Ideally, TCOs must possess high electrical conductivity, excellent optical transparency, and long-term stability. In addition, they should be composed of abundant elements, exhibit chemical and thermal stability under demanding fabrication conditions, and possess smooth surface morphology.[2,3,5,6] As such, TCOs with high optical transparency and electrical conductivity, such as fluorine-doped tin oxide (FTO) and indium tin oxide (ITO), have been widely employed in practical applications despite not being perfectly ideal, due to their sufficiently high performance.

FTO is an n-type material with a wide band gap, typically greater than 3.6 eV, and is heavily doped with fluorine. It exhibits excellent chemical stability and is composed solely of elements abundant on Earth. It also offers high carrier mobility, low resistivity ($\sim 3.7 \times 10^{-4}$ Ω cm), and high thermal stability (stable up to $\sim$700 °C). However, it has the drawback of high surface roughness ($R_a \sim$ 13.5 nm).[1,7,8] This roughness hinders effective contact with the semiconductor material and may result in poor charge transfer at the interface, thereby adversely affecting electrode efficiency. Despite this limitation, its above-mentioned advantages make it widely used in the fabrication of photoanodes for PEC cells.[9–11]

ITO, doped with indium, is an n-type degenerate semiconductor with a wide band gap of more than 3.5 eV. Among the TCOs, the ITO has the smoothest surface (<1 nm rms) and exhibits excellent transmittance (86.0% at 550 nm) in the visible light range. However, it contains indium as mentioned above, a very rare element, which leads to high production

[a] *Department of Chemistry, Chungbuk National University, Chungdae-ro 1, Cheongju, Chungbuk 28644, Korea. E-mail: nunyong@chungbuk.ac.kr; Tel: +82-43-261-2285*
[b] *Chungbuk National University G-LAMP Project Group, Chungdae-ro 1, Cheongju, Chungbuk 28644, Korea*
[c] *Department of Applied Chemistry, Faculty of Science and Technology, Chuo University, 1-13-27 Kasuga, Bunkyo, Tokyo 112-8551, Japan*

costs. Moreover, it has poor temperature stability (stable up to ~250 °C), leading to high resistance.[12–14] Nonetheless, it continues to be used in various PEC applications due to its smooth surface characteristics and high conductivity.[15–17]

This study aims to identify which of the two substrates, FTO or ITO, exhibits higher efficiency as a photoanode substrate in a PEC cell, and to investigate the underlying reasons for the difference in performance. Bismuth vanadate ($BiVO_4$) was used as the semiconductor material for the photoanode. In many studies, both FTO and ITO substrates have been widely employed for fabricating the $BiVO_4$-based photoanodes.[9,10,18–22] $BiVO_4$ is one of the materials widely used as a photoanode in PEC cells due to its narrow band gap (2.4–2.5 eV) and the appropriate energy position of its valence band (VB) edge, which provides a strong driving force for water oxidation.[23,24] The main methods for depositing $BiVO_4$ on conductive substrates include electrodeposition,[25–27] hydrothermal synthesis,[28,29] and the metal–organic decomposition (MOD) method.[9,30–32] Among these, we selected the MOD method to deposit $BiVO_4$ on FTO and ITO substrates in this study.

In this study, the F/B, in which $BiVO_4$ was deposited on FTO, exhibited a higher current density than the I/B, where $BiVO_4$ was deposited on ITO. To investigate the origin of efficiency differences depending on the substrate, various techniques were employed, including electrochemical measurements and spectroscopic methods such as pattern-illumination time-resolved phase microscopy (PI–PM) and near-field heterodyne transient grating (NF-HD-TG), which observe charge carrier dynamics. In particular, the NF-HD-TG method provides detailed information of the individual components of charge carrier dynamics within a photoelectrode and has been employed in several studies[33–35] to extract time constants for processes such as water oxidation and recombination. We also used this method to investigate charge carrier dynamics. The surface quality appeared to be better when $BiVO_4$ was grown on ITO than on FTO, as evidenced by the SEM images and photovoltage. However, the primary reason for the low current density observed in the I/B was identified as the poor junction between ITO and $BiVO_4$, which resulted in reduced charge separation efficiency and increased resistance. Nevertheless, NF-HD-TG measurements revealed that water oxidation occurred more rapidly in the I/B than in the F/B, which is likely attributable to its superior surface quality. This finding suggests that if thermal damage to the substrate can be minimized, ITO may offer greater suitability than FTO for photoelectrode applications.

2. Experimental

2.1 Synthesis

A $BiVO_4$ photoanode of monoclinic scheelite (MS) phase was fabricated *via* the MOD method.[9,30–32,36] The precursor was prepared with a 1 : 1 molar ratio of Bi to V (0.9 mmol each). Bismuth(III) nitrate pentahydrate ($Bi(NO_3)_3{\cdot}5H_2O$, Sigma-Aldrich) was completely dissolved in acetic acid (0.6 mol L^{-1}) and vanadyl acetylacetonate ($VO(acac)_2$, Sigma-Aldrich) was dissolved in acetylacetone (0.09 mol L^{-1}). The two solutions were mixed and stirred at 70 °C and 1500 rpm for over 30 minutes. The FTO (~7 Ω sq^{-1}, Sigma-Aldrich) and ITO (8–12 Ω sq^{-1}, Sigma-Aldrich) substrates were first washed with a synthetic detergent and then sonicated in a mixed solution of acetone and ethanol for 30 minutes. After spin-coating 260 μL of the $BiVO_4$ precursor at 2000 rpm for 20 seconds on each cleaned substrate, the film was annealed at 450 °C for 30 minutes in a furnace. This spin-coating and annealing process was considered one cycle, and this process was repeated 15 times. In the final step, an additional annealing was performed at 450 °C for 10 hours to achieve complete crystallization.

2.2 Characterization

Scanning electron microscopy (SEM, Carl Zeiss, Gemini 560) was used to analyze the film morphologies. In addition, the crystal structures of the films were confirmed by analyzing their X-ray diffraction (XRD) patterns using an X-ray diffractometer (Rigaku, Miniflex 600). UV-Vis absorption spectra were observed in the range of 400–800 nm using a UV-vis spectrophotometer (Agilent Technologies Cary 8454 UV-vis) to analyze the optical properties of the photoanodes. In addition, the elemental compositions of the samples were obtained using X-ray photoelectron spectroscopy (XPS, Ulvac-PHI, PHI Quantera-II).

2.3 PEC measurements

A potentiostat (CHI650E) was used to investigate the photoelectrochemical properties of the films under AM 1.5 G light provided by a solar simulator (100 mW cm^{-2}, Xe lamp). Photocurrent density–voltage curves (*J–V* curves), photocurrent density–time curves (*J–t* curves), photoelectrochemical impedance spectra (PEIS), open-circuit potentials (OCPs), and Mott–Schottky (M–S) plots were measured using the potentiostat. All PEC measurements were performed using a PEC cell equipped with a three-electrode system consisting of $BiVO_4$-based photoanode (working electrode), Pt (counter electrode), and Ag/AgCl (reference electrode), with 1 M potassium borate buffer solution (KBi, pH 9.0) as the electrolyte. The applied potential was converted to the reversible hydrogen electrode (RHE) scale using the Nernst equation below (eqn (1)), with $E^0_{Ag/AgCl}$ calculated as 0.197 V at 25 °C.

$$E_{RHE} = E_{Ag/AgCl} + 0.059pH + E^0_{Ag/AgCl} \quad (1)$$

Charge separation and transfer efficiencies were calculated using the following equations based on previous studies.[37,38]

$$\text{Photocurrent} = J_{abs} \times \eta_{sep} \times \eta_{trans} \quad (2)$$

$$\eta_{sep} = J_{Na_2SO_3}/J_{abs} \quad (3)$$

$$\eta_{trans} = J_{H_2O}/J_{Na_2SO_3} \quad (4)$$

$$J_{abs} = \frac{q}{hc}\int_{300}^{520} \lambda \Phi_\lambda \eta_{LHE} d\lambda \quad (5)$$

J_{abs} represents the photon absorption rate expressed as photocurrent density. It was calculated using eqn (5) according to a previous study,[37] and the wavelength range was set to 300–520 nm considering the band gaps of the samples. In eqn (5), q is the charge of an electron, while h and c represent the Planck constant and the speed of light, respectively. Here, Φ_λ corresponds to the photon flux of the AM 1.5 G solar spectrum, and η_{LHE} is the light harvesting efficiency. η_{sep} denotes the charge separation efficiency, and η_{trans} refers to the charge transfer efficiency. In the presence of a hole scavenger, η_{trans} is assumed to be 1, allowing eqn (3) to be derived from eqn (2). The photocurrent density measured in the presence of Na_2SO_3 ($J_{Na_2SO_3}$) was used to calculate η_{trans} using eqn (4), which is derived from eqn (2) and (3).

2.4 Time-resolved measurements

To investigate the dynamics of photo-excited charge carriers in photoanodes, we utilized the NF-HD-TG technique. The detailed principle of this method has been described in previous studies.[30,33,35,39–42] In brief, the third harmonic output of a Nd:YAG laser was used as the pump light (355 nm, 0.7 mJ per pulse, 10 Hz), and a continuous wave (CW) diode laser (638 nm) served as the probe light. The pump light was irradiated onto the films to generate a transient grating, and both signal and reference (0th order diffraction) were detected at the 0th order spot. By controlling the distance between the sample and the transmission grating, the signal intensity was optimized through interference between the signal and the reference. A photodiode (Thorlabs, PDA36A2) was used as the detector, with an edge filter (Semrock RazorEdge, LP02-355RU, 355 nm) and a long pass filter (Thorlabs, FELH0600, 600 nm) placed in front of it to remove the scattered pump light and fluorescence generated from the excited sample. The NF-HD-TG responses were monitored and recorded using an oscilloscope (Teledyne LeCroy, T3DSO3504). These measurements were performed at 0 V_{RHE} in 0.1 M phosphate buffer solution (KPi, pH 7) and at 1.4 V_{RHE} (in KBi, pH 9) using the same three-electrode system as employed in the PEC measurements.

The pattern-illumination time-resolved phase microscopy (PI–PM) method is a time-resolved pump–probe microscopy where the pump (355 nm, 0.5 mJ per pulse, 0.5 Hz) and probe light (532 nm, 0.02 mJ per pulse, 0.5 Hz) are collimated to illuminate the sample surface with a diameter of ~0.5 mm and the photo-excitation of charge carriers is observed *via* the phase-contrast imaging, namely a refractive index change by adjusting a slightly modified focus point.[43] Both the pump and probe lights are pulsed light with a pulse width of a few nanoseconds (3–4 ns), and the time-resolved image can be obtained by controlling the timing of the two pulses. An arbitrary pump light pattern is used to photo-excite charge carriers within the sample. These carriers are then subjected to processes such as charge trapping, recombination, and transfer. The spatial distribution of the photoexcited charge carriers is visualized. There are several key points to this method: the noisy image due to pulse-laser imaging is recovered by mathematical and statistical calculations called ''total-variation regularization'' and the pattern-illumination is used for this purpose, and this mathematical procedure naturally connects the spatial and temporal tensor data and recovers the image sequence using a penalty term that sums the derivatives in the spatial and temporal directions;[44] the carriers trapped at the surface/defect states are efficiently observed through changes in the refractive index, which are not observed directly by the transient absorption or time-resolved photoluminescence; different types of carriers on a surface are distinguished by the sign of the refractive index change and the distribution change by the carrier scavengers contacting *via* the solution interface. A sample film on a substrate was sandwiched by another glass substrate with a rubber spacer (thickness; 0.5 mm). An amount of 0.15 mL of liquid was introduced into the gap layer. Each sample was measured in contact with acetonitrile (ACN), ethanol (EtOH), and a solution of 0.1 mM nitrobenzene in EtOH (NB/EtOH), respectively. ACN was used as an inert solution to prevent charge transfer from the photocatalytic materials to the liquid. EtOH was used as a hole scavenger, while the NB/EtOH served as a scavenger for both electrons and holes.

3. Results and discussion

XRD patterns, as shown in Fig. 1, were measured to confirm the crystallinities of the films. The at symbol (@) indicates a diffraction peak originating from the SnO_2 of the FTO substrate,[45,46] and the asterisk (*) sign corresponds to the In_2O_3 peak from the ITO substrate.[47,48] The hash (#) sign represents the $BiVO_4$ in the MS phase.[9,49] These results confirm that $BiVO_4$ was successfully synthesized on both the FTO and ITO substrates.

The surface morphologies of each film were examined using SEM. The cross-sectional SEM images of the films, provided in Fig. S1 in the SI, show that the $BiVO_4$ layer has a thickness of approximately 200 nm on both substrates. Additionally, as shown in Fig. 2, typical $BiVO_4$ morphology was observed on

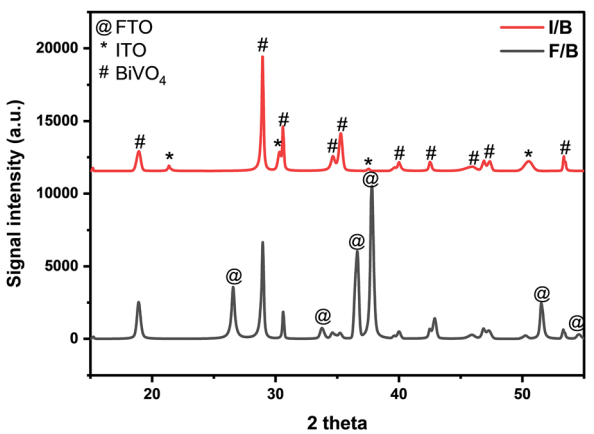

Fig. 1 XRD patterns of F/B (black) and I/B (red) films. The at (@) sign corresponds to the diffraction peaks arising from SnO_2 of the FTO substrate (JCPDS No. 01-079-6887), the asterisk (*) indicates the diffraction peaks of In_2O_3 originating from the ITO substrate (JCPDS No. 01-089-4597) and the hash (#) corresponds to the $BiVO_4$ (JCPDS No. 14-0688).

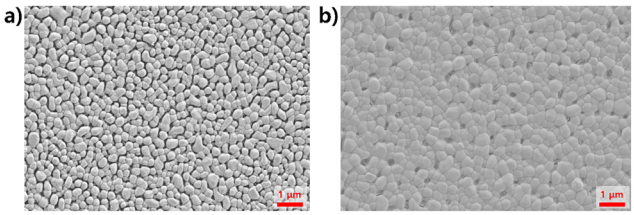

Fig. 2 SEM images of the (a) the F/B and (b) the I/B films.

both substrates, although the particle arrangement differed. The F/B exhibited well-defined $BiVO_4$ particles with visible pores, while the I/B showed a more densely packed and continuous structure. Namely, the I/B exhibited a lower degree of surface porosity compared to the F/B. As excessive porosity can allow the electrolyte to penetrate through to the substrate, which negatively impact cell performance,[50] the reduced porosity in the I/B may be beneficial.

To investigate whether the absorption properties of $BiVO_4$ are influenced by the choice of substrate, UV-vis absorption spectra were measured, as shown in Fig. 3a. The corresponding Tauc plots, derived from these spectra, are presented in Fig. 3b. As shown in Fig. 3, the absorption characteristics of $BiVO_4$ were not significantly affected by the use of either FTO or ITO substrates. To obtain reliable direct band gap values, we applied an proper extrapolation (PE) method[51,52] to fit the Tauc plots. The direct band gap[24,53] values were consistent with the theoretical direct band gap of the $BiVO_4$ (2.4–2.5 eV).

To analyze the chemical and electronic environments of the film surfaces, XPS measurements were conducted. As shown in the XPS survey spectra in Fig. S2 in the SI, the presence of Bi, V, and O peaks confirmed that $BiVO_4$ was successfully deposited on both substrates. In Fig. 4a and b, Bi 4f peaks were observed at binding energies of approximately 164.6 eV (Bi $4f_{5/2}$) and 159.3 eV (Bi $4f_{7/2}$) for both the F/B and the I/B. Similarly, V 2p peaks appeared at around 524.4 eV (V $2p_{1/2}$) and 516.9 eV (V $2p_{3/2}$), as shown in Fig. 4c and d. The O 1s spectra in Fig. 4e and f displayed signals corresponding to lattice oxygen (O_L), oxygen vacancies (O_V), and chemisorbed oxygen species (O_A),[54,55] observed at 530, 531.4, and 532.5 eV, respectively. Detailed information from the XPS spectra (*e.g.*, binding energies, intensities, and FWHM) is presented in Tables S1 and S2 in the SI. Based on the Bi 4f and V 2p spectra, we were able to confirm once again that $BiVO_4$ was successfully grown on both FTO and ITO substrates, with no chemical shift observed in the XPS spectra. In the O 1s spectra, the intensity of O_V was observed to be higher in F/B than in I/B, indicating that I/B possesses fewer active sites.

To assess the PEC performances of each sample, linear sweep voltammetry (LSV) was conducted to obtain *J–V* curves. From these measurements, both the onset potential and photocurrent density were determined. As illustrated in Fig. 5a, the F/B showed a current density of 0.671 mA cm^{-2} at 1.23 V_{RHE}, whereas the I/B exhibited 0.210 mA cm^{-2}. In terms of onset potential, the F/B demonstrated a value of 0.509 V_{RHE}, while the I/B displayed 0.687 V_{RHE}. Based on a previous study,[56] the onset potential was defined as the point at which the first derivative of the *J–V* curves first reached 0.2 mA cm^{-2}. Since the I/B exhibited a higher onset potential and lower current density compared to the F/B, it clearly indicates that $BiVO_4$ deposited on FTO offers significantly better PEC performance than on the ITO.

Fig. 5b shows the *J–t* curves measured to evaluate the stabilities of the samples. The measurements were conducted at 0.8 V_{RHE} based on conditions from a previous study,[57] using a 1 M KBi buffer solution (pH 9), which was also used in all PEC measurements. The photocurrent density of the F/B decreased for approximately 1000 s and then increased, while that of the I/B rapidly decreased within about 300 s and subsequently increased gradually. According to X. Cao *et al.*, the initial decrease is attributed to the dissolution of V^{5+}, while the subsequent increase results from a photoactivation process.[57] The faster current decay in the I/B indicates a more rapid V^{5+} dissolution, suggesting that its stability is lower than that of the F/B. Furthermore, the photoactivation effect appears to be more prominent in the F/B. This suggests that additional consideration of the electrolyte is required when employing ITO for $BiVO_4$.

Applied bias photon-to-current efficiencies (ABPEs) were calculated based on the LSV data using the equation described

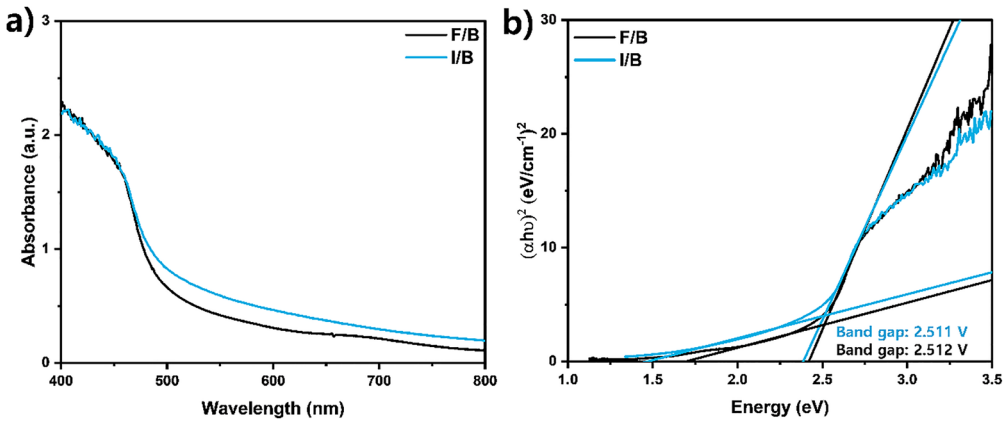

Fig. 3 (a) Absorption spectra obtained from UV-vis measurements in the 400–800 nm range, and (b) the Tauc plots of the F/B and the I/B films.

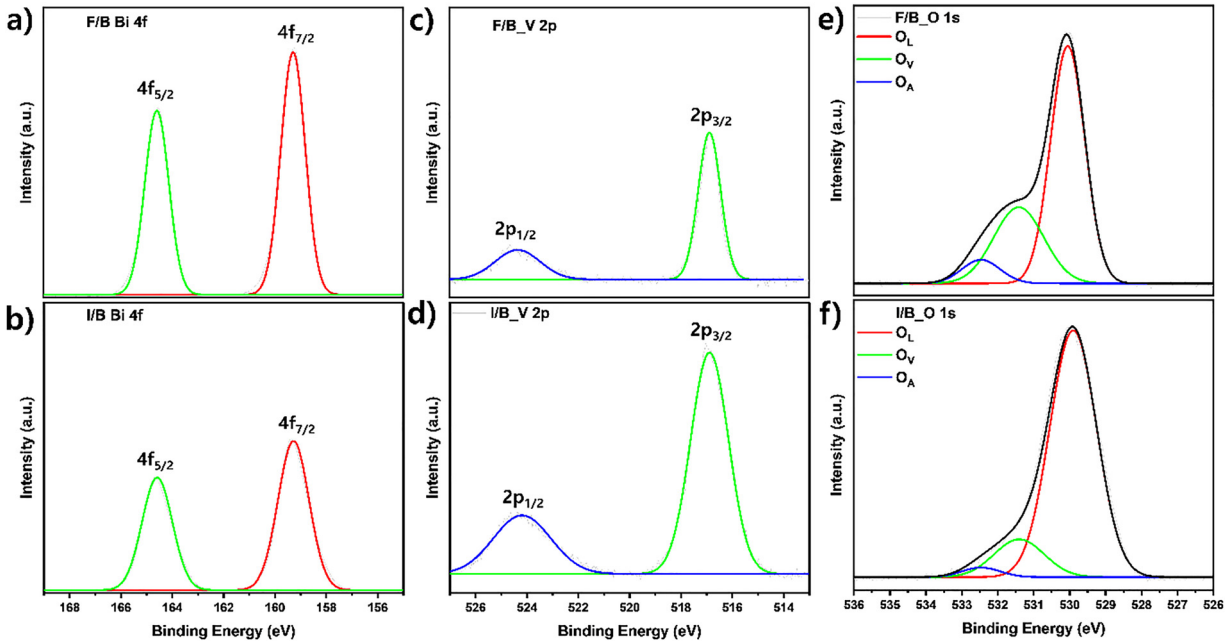

Fig. 4 XPS spectra with fitting curves (narrow scan) for (a) Bi 4f in F/B, (b) Bi 4f in I/B, (c) V 2p in F/B, (d) V 2p in I/B, (e) O 1s in F/B, and (f) O 1s in I/B.

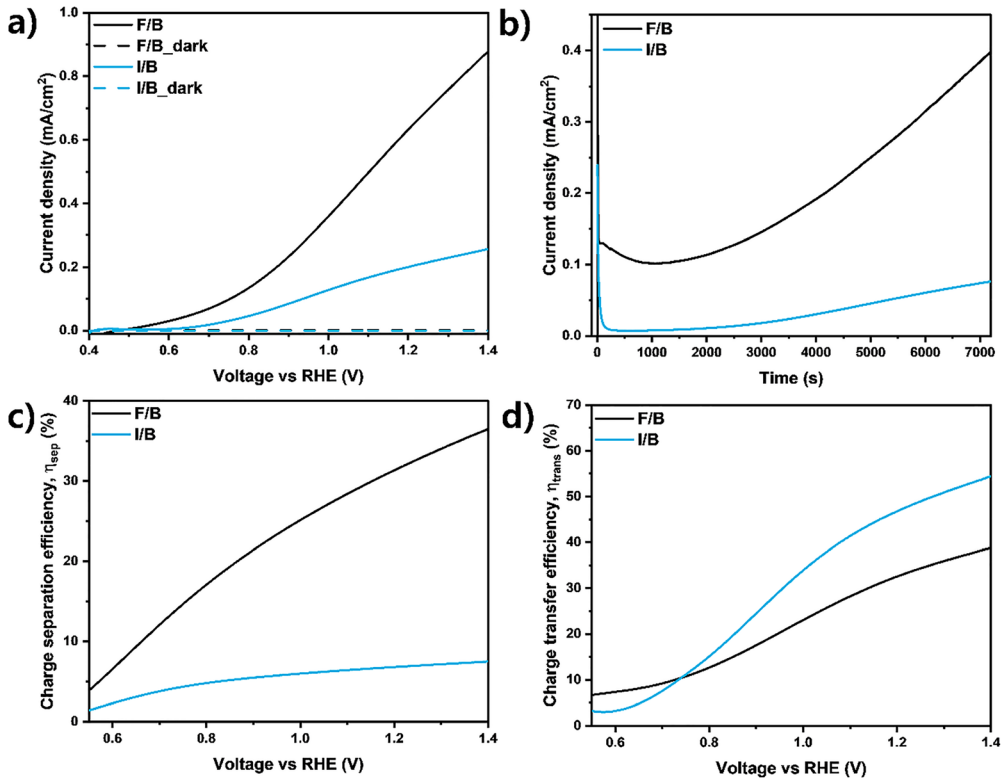

Fig. 5 (a) *J*–*V* curves obtained *via* linear sweep voltammetry (LSV) under illumination (solid lines) and in the dark (dotted lines), (b) *J*–*t* curves measured at 0.8 V_{RHE}, (c) charge separation and (d) transfer efficiencies measured in the presence of hole scavenger (Na_2SO_3) in the electrolyte. Data for the F/B (black) and the I/B (blue) films.

in a previous study.[58,59] As shown in Fig. S3 in the SI, the ABPE% of the F/B was observed to be higher than that of the I/B (F/B: 0.083%, I/B: 0.029% at 1.0 V_{RHE}).

To evaluate the charge separation and transfer efficiencies of the films, *J*–*V* curves were measured in the presence of the hole scavenger Na_2SO_3 (Fig. S4 in the SI). As shown in Fig. 5c and d,

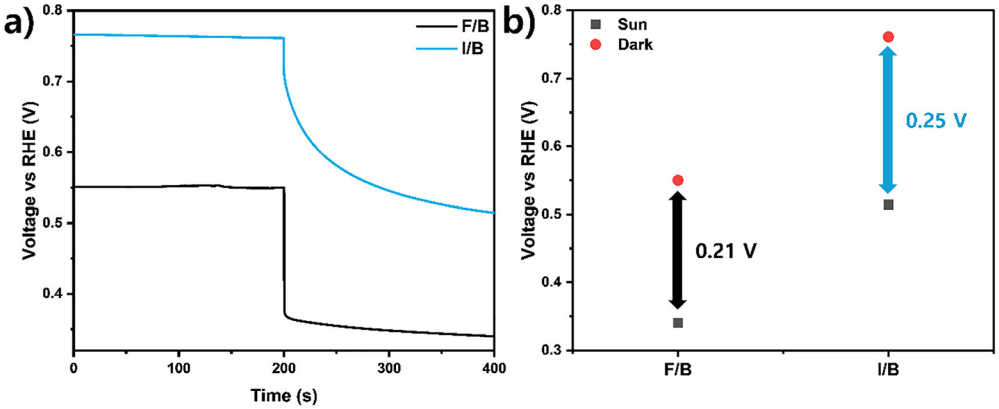

Fig. 6 (a) OCP *vs.* time plots of F/B (black) and I/B (blue) measured for 200 s each under dark and illumination conditions. (b) OCP values and photovoltages under dark (red circle) and illumination (grey square) conditions.

the efficiencies were calculated using the eqn (2)–(4). The J_{abs} values were 6.200 mA cm^{-2} and 6.307 mA cm^{-2} for the F/B and I/B, respectively. In the terms of charge separation efficiency (Fig. 5c), the F/B exhibited significantly higher efficiency than the I/B across the entire applied voltage range (0.55–1.4 V_{RHE}), indicating that photogenerated carriers in the bulk of the I/B were not effectively separated. This inefficiency may be attributed to the poor junction between ITO and $BiVO_4$, which could have induced Fermi level pinning and consequently reduced the charge separation efficiency.

In contrast, for the charge transfer efficiency (Fig. 5d), the I/B exhibited lower efficiency than the F/B at relatively low applied voltages, but an inversion occurred at higher voltages, where the I/B exhibited better transfer efficiency. At relatively low voltages, the I/B exhibited poor charge separation and transfer efficiencies, which likely explains its higher onset potential. However, at higher applied voltages, the improved transfer efficiency in the I/B may result from differences in the $BiVO_4$ growth conditions depending on the substrate. This enhancement suggests that $BiVO_4$ exhibits superior surface quality on ITO compared to FTO, as supported by the SEM images.

The OCPs measured under dark and illumination conditions (Fig. 6) were used to determine the photovoltage of the films. The photovoltage, defined as the difference between the OCP values under dark and illuminated conditions, was observed to be larger for the I/B. This suggests that the space charge layer was more effectively generated in the I/B than in the F/B, indicating that the interfacial junction between the $BiVO_4$ surface and the electrolyte is more favorable when $BiVO_4$ is deposited on ITO under unbiased conditions. This result provides additional evidence that the surface quality of $BiVO_4$ is enhanced when grown on ITO. In addition, the slower voltage decay observed in the I/B upon light-off further indicates that the space charge layer is more effectively formed in the I/B (Tables 1 and 2).

Fig. 7 shows the M–S plots of each sample measured under dark conditions at 500 Hz. The flat band potential (V_{FB}) was determined from the *x*-intercept of the M–S plot, and the donor density was calculated using the following eqn (6).[60] In this equation, N_D represents the donor density, V is the applied potential, and ε_r is the relative permittivity[61] (68 for $BiVO_4$). The V_{FB} and N_D values are summarized in Table 1.

Table 1 List of flat band potentials (V_{FB}) and donor densities (N_D) of the F/B and the I/B films

	V_{FB}	$N_D/10^{18}$ cm^{-3}
F/B	0.71	2.18
I/B	0.58	3.03

Table 2 The resistance values of the F/B and the I/B films. (R_s: the resistance between the conductive substrate and the semiconductor, R_1: the resistance in the bulk, and R_2: the resistance between the semiconductor and the electrolyte)

	R_s (Ω)	R_1 (Ω)	R_2 (Ω)
F/B	112.1	111.9	1390
I/B	249.3	251.3	35 733

$$N_D(\mathrm{cm}^{-3}) = \frac{1.41 \times 10^{32}(\mathrm{cm} \times \mathrm{F}^{-2} \times \mathrm{V}^{-1})}{\varepsilon_r \times A^2(\mathrm{cm}^4) \times \mathrm{slop}(\mathrm{F}^{-2} \times \mathrm{V}^{-1})} \quad (6)$$

The V_{FB} is closely related to the onset potential; generally, a lower V_{FB} corresponds to a lower onset potential. However, although the I/B exhibited a lower V_{FB} compared to the F/B, it showed a higher onset potential, as shown in Fig. 5a. According to a previous study,[60] photovoltage and water oxidation kinetics can influence the V_{FB}. In the case of the I/B, the large difference between the onset potential and V_{FB} may be due either to an insufficient number of surface-trapped holes or to a low-rate constant for water oxidation.

The N_D was found to be higher in the I/B, which may be one of the causes of Fermi level pinning. Due to Fermi level pinning, charge carriers could not be effectively separated, which is consistent with the charge separation efficiency results shown in Fig. 5c, likely leading to the lower PEC performance observed in the I/B.

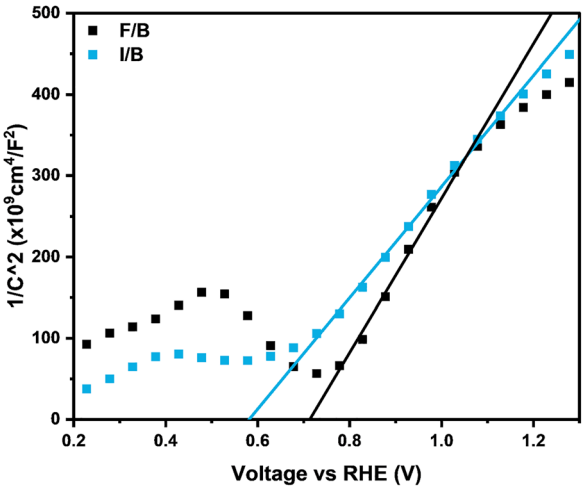

Fig. 7 M–S plots of F/B (black) and I/B (blue) films, measured in an aqueous solution under the dark condition at 500 Hz.

PEIS was conducted to investigate the transport and transfer kinetics of charge carriers by analyzing the resistance values at interface. Fig. 8 presents the Nyquist plots of the F/B and the I/B, with the inset displaying the equivalent circuit diagram used for fitting. In this model, R_s represents the overall series resistance of the circuit, R_1 corresponds to the bulk resistance, and R_2 denotes the interfacial resistance between the semiconductor and the electrolyte. The resistance values for each film are listed in Table 2.

R_s is associated with the junction quality of the film; when the contact between the conductive substrate and the semiconductor is inadequate, R_s tends to increase. A significantly larger R_s was observed for the I/B, suggesting that the junction at the ITO/$BiVO_4$ interface was not properly formed. As a result of this poor contact, the charge separation efficiency was also diminished as shown in Fig. 5c. Since ITO is thermally less stable, repeated processing at high temperatures (450 °C) may have damaged the substrate. This, in turn, likely impaired its ability to form a proper junction with $BiVO_4$, resulting in a poorly formed interfacial contact between ITO and the $BiVO_4$.

R_1 is related to the bulk conductivity, while R_2 corresponds to the hole transfer efficiency. In agreement with the charge separation efficiency results, the F/B exhibited better conductivity than the I/B, which showed a higher R_1 value. Although the I/B exhibited better surface quality, its higher R_1 and R_2 were likely due to the poor interfacial junction and inefficient charge separation, which may have resulted in a lower concentration of surface-trapped holes or a smaller reaction rate constant for water oxidation.

Based on the SEM images and photovoltage results, the surface quality of $BiVO_4$ appears to be superior when deposited on ITO. However, the poor junction between ITO and $BiVO_4$ seems to have degraded the bulk quality of the film. This is considered the main factor limiting the performance of the I/B, despite its other favorable properties.

The PI–PM method was applied for the F/B and I/B. This method monitors the density change of the trapped charge carriers after the free charge carriers (electrons and holes) at the conduction and valence bands are trapped to the surface/defect states, followed by recombination. This technique analyzes locally trapped charge carrier responses with the micron-level resolution to provide distinct responses for electrons and holes,[62] which can be confirmed by the scavenger effect (Fig. S5 and S6 in the SI, for the F/B and I/B, respectively). Fig. 9 shows the comparison of the trapped charge carrier behavior between

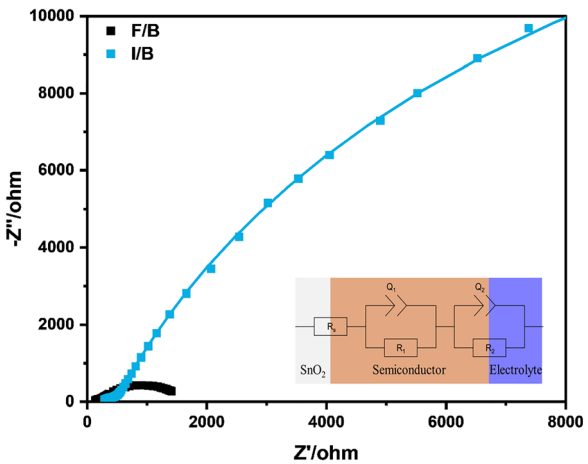

Fig. 8 The Nyquist plots of the F/B (black) and the I/B (blue), measured at 0.5 V_{RHE}; the inset displays the equivalent circuit diagram used for fitting.

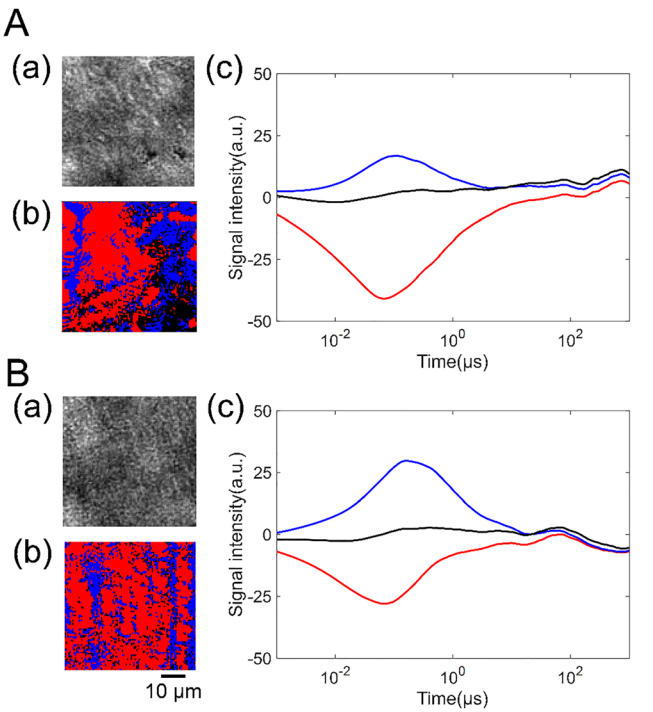

Fig. 9 The PI–PM analysis results for the (A) F/B and (B) the I/B, respectively. (a) Corresponds to a microscopic image, and the corresponding categorized map is shown in (b), and the scale bar corresponds to 10 μm. The averaged responses for the categorized responses are shown in (c).

F/B and I/B. Both the F/B and I/B exhibited two types of responses: positive (electron) and negative (hole). Both charge carriers decayed for 0.3–1.3 microseconds. After checking several different regions, the decay times of the holes and electrons for the I/B became faster and slower than those of the F/B (the hole decay time: 0.6 to 0.3 μs; the electron decay time: 0.7 to 1.3 μs), and the electron response for the F/B surface was much weaker than that of the I/B.

The result indicates that the electrons are transferred to an FTO substrate more smoothly, which caused the signal response to be smaller. On the other hand, more electrons remained for I/B and trapped in the surface states, causing the slower decay. This suggests that the electrons were not efficiently transferred to the ITO substrate, which is likely due to the poor junction between the ITO and the $BiVO_4$, consistent with the higher R_s.

NF-HD-TG responses were measured in KPi (pH 7) at 0 V_{RHE} and in KBi (pH 9) at 1.4 V_{RHE} to investigate the dynamics of photo-generated holes and electrons in the F/B and I/B. Under the 0 V_{RHE} condition, water oxidation does not occur;[63,64] thus, the slow decay of long-lived holes can be attributed to recombination. The NF-HD-TG responses measured at 0 V_{RHE}, along with the corresponding fitting curves, are shown in Fig. 10a and b. In contrast, at 1.4 V_{RHE}, where water oxidation occurs,[65] the slow decay of long-lived holes is likely associated with water oxidation process. Fig. 10c and d display the NF-HD-TG responses measured at 1.4 V_{RHE} accompanied by the corresponding fitting curves. The observed responses at 0 V_{RHE} were fitted using a combination of a power-law function and two exponential functions, as described by eqn (7). For the responses at 1.4 V_{RHE}, eqn (8), combines a power-law function with three exponential functions, was employed to include the third exponential function.

$$I(t) = at^{-b} + A_1e^{-t/\tau_1} + A_2e^{-t/\tau_2} \quad (7)$$

$$I(t) = at^{-b} + A_1e^{-t/\tau_1} + A_2e^{-t/\tau_2} + A_3e^{-t/\tau_3} \quad (8)$$

The fast decay component, fitted by the power-law function (at^{-b}), was assigned to bimolecular recombination, which refers to the recombination between holes in the space charge layer in the VB and free electrons in the conduction band (CB).[31,66,67] The second (A_1e^{-t/τ_1}) and third (A_2e^{-t/τ_2}) components were fitted using exponential functions and attributed to thermal diffusion and trap-mediated recombination, respectively.[9,30,68] These components appeared identically under both 0 and 1.4 V_{RHE} conditions; however, at 1.4 V_{RHE}, an additional third component (A_3e^{-t/τ_3}) appeared, which was fitted using an exponential function and assigned to water oxidation.[9,30,68] To distinguish these components, NF-HD-TG responses were compared for grating spacings (Λ) of 30 μm (Fig. 10) and 70 μm (Fig. S7 in the SI). As shown in Table 3 and Table S3 in the SI, one decay component showed strong dependence on the Λ, while the other did not. The second component that varied with Λ was assigned to thermal diffusion. The third component was identified as the trap-mediated

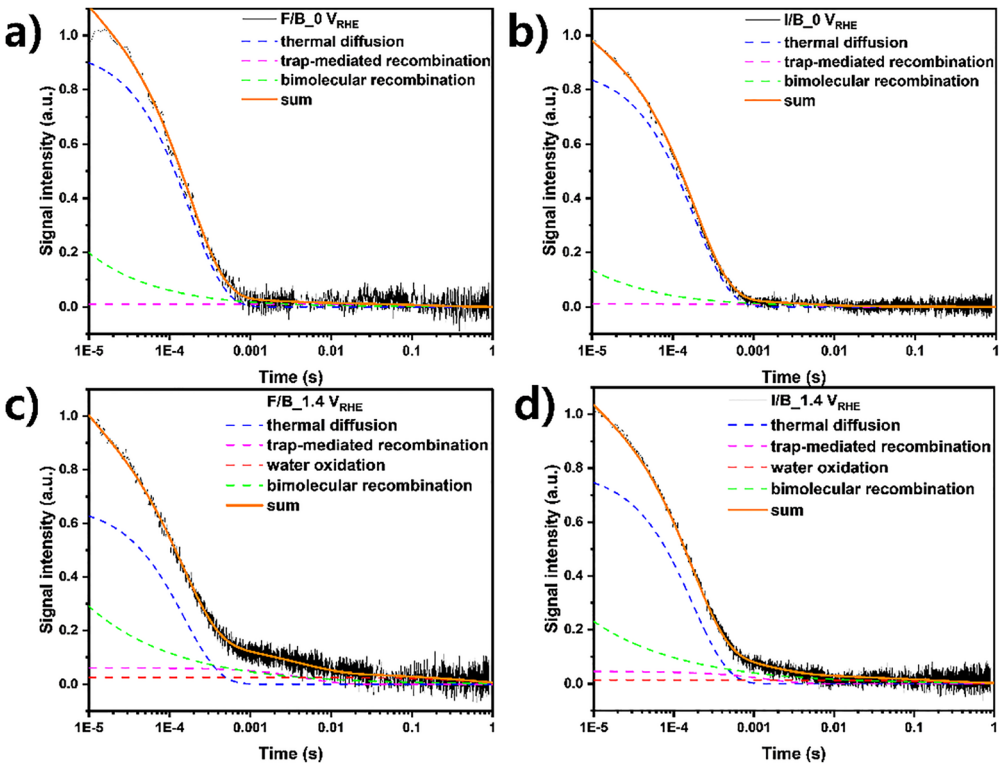

Fig. 10 NF-HD-TG responses of (a) the F/B, (b) the I/B at 0 V_{RHE}, (c) the F/B, and (d) the I/B at 1.4 V_{RHE} at the grating spacing (Λ) of 30 μm with fitting curves.

Table 3 List of the time constants of the F/B and the I/B films at 0 V_{RHE} at the grating spacing of 30 μm

	τ_1 ($\times 10^{-4}$ s)	τ_2 ($\times 10^{-2}$ s)
F/B	1.8	20.0
I/B	1.88	0.61

recombination, referring to the recombination between free electrons in the CB and holes trapped at the surface. As confirmed by the PI–PM and charge separation efficiency results, electron transfer from $BiVO_4$ to ITO is hindered in the I/B. Consequently, a greater number of electrons remain in the CB rather than being transferred to the substrate, increasing the likelihood of recombination with surface-trapped holes and thus supporting the assignment to the trap-mediated recombination. As shown in Tables 3 and 4, the rate constant of the trap-mediated recombination in the F/B was 0.2 s at 0 V_{RHE} and 0.00503 s at 1.4 V_{RHE}, while it in the I/B was 0.0061 s at 0 V_{RHE} and 0.00151 s at 1.4 V_{RHE}. This indicates that the trap-mediated recombination occurs more rapidly in the I/B, which may contribute to its lower current density. Consistent with the PI–PM results, the faster recombination is likely due to inefficient electron transfer to the ITO substrate, thereby increasing the probability of recombination with surface-trapped holes. According to Table 4, the water oxidation time constant was 0.553 s for the F/B and 0.281 s for the I/B. The faster water oxidation in the I/B was consistent with the higher charge transfer efficiency shown in Fig. 5d. XPS results (Fig. 4e and f) indicate that the number of active sites in I/B was lower than in F/B; however, the number of active sites is not the sole factor determining the charge transfer rate. Despite having fewer active sites in which fewer photo-generated holes could be trapped, effective water oxidation was still observed in I/B, suggesting that the superior surface quality of $BiVO_4$ grown on the ITO enables more efficient water oxidation.

Table 4 List of the time constants of the F/B and the I/B films at 1.4 V_{RHE} at the grating spacing of 30 μm

	τ_1 ($\times 10^{-4}$ s)	τ_2 ($\times 10^{-3}$ s)	τ_3 (s)
F/B	1.52	5.03	0.553
I/B	1.75	1.51	0.281

The summary of this study is illustrated in the schematic diagram in Fig. 11. As shown in the SEM images in Fig. 2, $BiVO_4$ grown on the ITO substrate exhibited fewer pores, indicating a denser surface structure. Furthermore, the OCP results in Fig. 6 showed that the I/B had a higher photovoltage and NF-HD-TG results indicated that the water oxidation occurred significantly faster in the I/B. These consistent observations—a denser surface structure, higher photovoltage, and markedly faster water oxidation—strongly demonstrate that the I/B possesses superior surface quality compared to the F/B. However, as demonstrated by the *J–V* curves in Fig. 5a, the overall PEC performance of the I/B was significantly lower. This was mainly attributed to the poor interfacial contact between ITO and $BiVO_4$, as evidenced by the high R_s observed in the PEIS (Fig. 8). This unfavorable junction impeded efficient charge separation (Fig. 5c) and hindered electron transfer to the ITO substrate, as indicated by the PI–PM results (Fig. 9). Moreover, the NF-HD-TG results revealed that the trap-mediated recombination occurs much more rapidly in the I/B, which likely contributed to its lower current density. As mentioned in the introduction, ITO has poor thermal stability, and the repeated high-temperature annealing steps required in the MOD process for $BiVO_4$ deposition are likely to damage the substrate, resulting in a degraded interfacial junction between ITO and $BiVO_4$. Therefore, although growing $BiVO_4$ on the ITO substrate can result in a better surface, its PEC performance was found to be significantly lower than that of the F/B. If a method can be developed to deposit $BiVO_4$ without damaging the ITO substrates, it is expected that ITO could potentially outperform FTO. There are, in fact, several reported studies[18,20,69] in which ITO has been successfully used as a conductive substrate for $BiVO_4$. These reports suggest that, with careful adjustment of the annealing temperature and number of cycles, ITO may serve as a promising substrate for constructing $BiVO_4$ photoanodes more effectively.

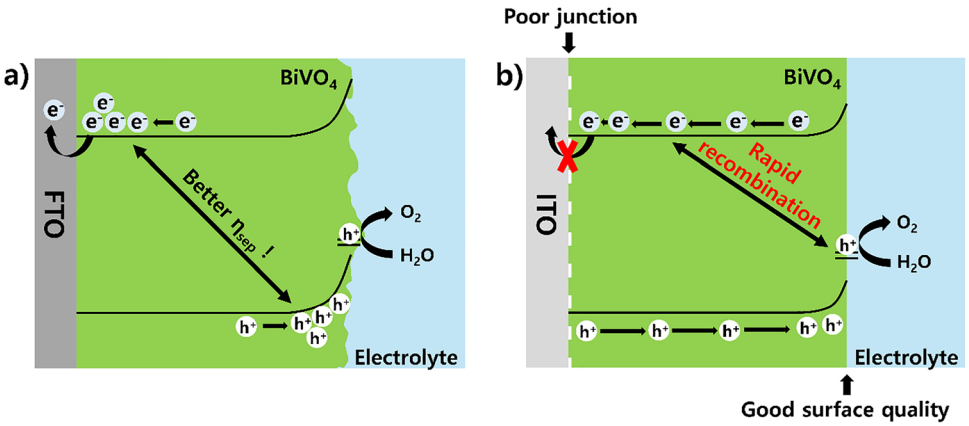

Fig. 11 Schematic diagram of (a) F/B and (b) I/B.

4. Conclusion

In this study, we fabricated $BiVO_4$ films on both FTO and ITO substrates to compare their PEC performance and investigate the underlying causes of the observed differences. We found that the F/B exhibited a higher current density and lower onset potential compared to the I/B, which was attributed to the poor interfacial junction between the ITO and $BiVO_4$. While the SEM image, photovoltage and water oxidation time constant suggest that the surface quality of the $BiVO_4$ is better when grown on the ITO, repeated high temperature annealing likely damaged the ITO substrate, resulting in a degraded interface between the ITO and the $BiVO_4$. This led to significantly reduced charge separation efficiency and increased overall resistance in the electrode. Indeed, charge carrier dynamics analysis revealed that electrons were not efficiently transferred to the ITO substrate, remaining in the CB and recombining with surface-trapped holes. As a result, these trapped holes were not effectively utilized for water oxidation. This issue could potentially be addressed by employing a deposition method that requires only a single annealing step, such as electrodeposition,[26] sol–gel method,[70] and spray pyrolysis.[71]

Conflicts of interest

There are no conflicts to declare.

Data availability

The data supporting this article have been included as part of the supplementary information (SI). Supplementary information: cross-sectional SEM images, XPS survey spectra, tables of XPS peak parameters, ABPEs, *J–V* curves in presence of Na_2SO_3, clustering analyses, NF-HD-TG responses with the grating spacings (Λ) of 70 μm. See DOI: **https://doi.org/10.1039/d5ma01153a**.

Acknowledgements

The work was supported by Global – Learning & Academic research institution for Master's PhD students, and Postdocs (G-LAMP) Program of the NRF grant funded by the Ministry of Education (RS-2024-00445180).

References

1 W. Xu, C. Zhen, J. Qiu, Y. Du, S. Bai, H.-M. Cheng and G. Liu, *Sci. China Mater.*, 2023, **66**, 4663–4668.
2 D. S. Ginley and C. Bright, *MRS Bull.*, 2000, **25**, 15–18.
3 P. D. C. King and T. D. Veal, *J. Phys.: Condens. Matter*, 2011, **23**, 334214.
4 M. Sharma, D. Chaudhary, N. Dwivedi, S. Sudhakar and S. Kumar, *Silicon*, 2017, **9**, 59–68.
5 D. A. Keller, H.-N. Barad, E. Rosh-Hodesh, A. Zaban and D. Cahen, *MRS Commun.*, 2018, **8**, 1358–1362.
6 T. Qiu, E. M. Akinoglu, B. Luo, M. Konarova, J.-H. Yun, I. R. Gentle and L. Wang, *Adv. Mater.*, 2022, **34**, 2103842.
7 H. Zhao, J. Kiwi, C. Pulgarin and J. Yang, *Int. J. Appl. Glass Sci.*, 2013, **4**, 242–247.
8 G. Rey, C. Ternon, M. Modreanu, X. Mescot, V. Consonni and D. Bellet, *J. Appl. Phys.*, 2013, **114**, 183713.
9 J. Y. Won, Z. Pan, Y. Pihosh and W. Y. Sohn, *Int. J. Hydrogen Energy*, 2024, **54**, 1544–1551.
10 Q. Wang, J. He, Y. Shi, S. Zhang, T. Niu, H. She and Y. Bi, *Chem. Eng. J.*, 2017, **326**, 411–418.
11 Y. G. Shim, J. Y. Ko, J. H. Kim, S. H. Jeong and W. Y. Sohn, *J. Photochem. Photobiol., A*, 2025, **464**, 116303.
12 Y.-N. Kim, H.-G. Shin, J.-K. Song, D.-H. Cho, H.-S. Lee and Y.-G. Jung, *J. Mater. Res.*, 2005, **20**, 1574–1579.
13 C. C. Wu, C. I. Wu, J. C. Sturm and A. Kahn, *Appl. Phys. Lett.*, 1997, **70**, 1348–1350.
14 M. H. Sohn, D. Kim, S. J. Kim, N. W. Paik and S. Gupta, *J. Vac. Sci. Technol., A*, 2003, **21**, 1347–1350.
15 T. Minami, *Thin Solid Films*, 2008, **516**, 5822–5828.
16 J. Gil-Rostra, J. Castillo-Seoane, Q. Guo, A. B. Jorge Sobrido, A. R. González-Elipe and A. Borrás, *ACS Appl. Mater. Interfaces*, 2023, **15**, 9250–9262.
17 T. Hong, Z. Liu, X. Zheng, J. Zhang and L. Yan, *Appl. Catal., B*, 2017, **202**, 454–459.
18 H. Luo, A. H. Mueller, T. M. McCleskey, A. K. Burrell, E. Bauer and Q. X. Jia, *J. Phys. Chem. C*, 2008, **112**, 6099–6102.
19 S. Hernández, G. Saracco, G. Barbero and A. L. Alexe-Ionescu, *J. Electroanal. Chem.*, 2017, **799**, 481–486.
20 Y. Pihosh, I. Turkevych, K. Mawatari, T. Asai, T. Hisatomi, J. Uemura, M. Tosa, K. Shimamura, J. Kubota, K. Domen and T. Kitamori, *Small*, 2014, **10**, 3692–3699.
21 Y. An, C. Lin, C. Dong, R. Wang, J. Hao, J. Miao, X. Fan, Y. Min and K. Zhang, *ACS Energy Lett.*, 2024, **9**, 1415–1422.
22 C. Dong, Y. Yang, X. Hu, Y. Cho, G. Jang, Y. Ao, L. Wang, J. Shen, J. H. Park and K. Zhang, *Nat. Commun.*, 2022, **13**, 4982.
23 W. Zhou, T. Jiang, Y. Zhao, C. Xu, C. Pei and H. Xue, *J. Alloys Compd.*, 2019, **777**, 1152–1158.
24 A. Walsh, Y. Yan, M. N. Huda, M. M. Al-Jassim and S.-H. Wei, *Chem. Mater.*, 2009, **21**, 547–551.
25 T. W. Kim and K.-S. Choi, *Science*, 2014, **343**, 990–994.
26 N. A. Mohamed, N. A. Arzaee, M. F. Mohamad Noh, A. F. Ismail, J. Safaei, J. S. Sagu, M. R. Johan and M. A. Mat Teridi, *Ceram. Int.*, 2021, **47**, 24227–24239.
27 K. Zhang, J. Liu, L. Wang, B. Jin, X. Yang, S. Zhang and J. H. Park, *J. Am. Chem. Soc.*, 2020, **142**, 8641–8648.
28 S. Obregón, A. Caballero and G. Colón, *Appl. Catal., B*, 2012, **117–118**, 59–66.
29 Z. R. Rhoomi, D. S. Ahmed, M. S. Jabir, B. Balasubramanian, M. A. Al-Garadi and A. A. Swelum, *ACS Omega*, 2023, **8**, 37147–37161.
30 A. Minato, Z. Pan, K. Katayama and W. Yong Sohn, *J. Photochem. Photobiol., A*, 2023, **434**, 114252.
31 Y. Ma, S. R. Pendlebury, A. Reynal, F. Le Formal and J. R. Durrant, *Chem. Sci.*, 2014, **5**, 2964–2973.

32 J. H. Kim, S. H. Jeong, A. Hong, Z. Pan, K. Katayama and W. Y. Sohn, *Bull. Korean Chem. Soc.*, 2025, **46**, 301–309.
33 Y. H. Kim, Y. G. Bae and W. Y. Sohn, *Phys. Chem. Chem. Phys.*, 2023, **25**, 11981–11985.
34 S. K. Jang, S. H. Jeong, A. Hong and W. Y. Sohn, *J. Phys. Chem. Lett.*, 2025, **16**, 9993–9999.
35 Y. H. Kim, Y. G. Bae, M. H. Lee, J. Kim and W. Y. Sohn, *J. Phys. Chem. C*, 2024, **128**, 2990–2996.
36 A. Galembeck and O. L. Alves, *Thin Solid Films*, 2000, **365**, 90–93.
37 B. Liu, X. Wang, Y. Zhang, K. Wan, L. Xu, S. Ma, R. Zhao, S. Wang and W. Huang, *Adv. Energy Mater.*, 2025, **15**, 2403835.
38 H. Dotan, K. Sivula, M. Grätzel, A. Rothschild and S. C. Warren, *Energy Environ. Sci.*, 2011, **4**, 958–964.
39 M. Okuda and K. Katayama, *Chem. Phys. Lett.*, 2007, **443**, 158–162.
40 K. Katayama, K. Sato, H. Sugiya and T. Shoji, *Chem. Phys. Lett.*, 2009, **479**, 306–309.
41 M. Yamaguchi, K. Katayama, Q. Shen, T. Toyoda and T. Sawada, *Chem. Phys. Lett.*, 2006, **427**, 192–196.
42 Y. Hyun Kim, Y. Gyeong Bae and W. Yong Sohn, *ChemPhysChem*, 2024, **25**, e202300894.
43 K. Katayama, *Phys. Chem. Chem. Phys.*, 2024, **26**, 9783–9815.
44 X. Huang, J. Fan, L. Li, H. Liu, R. Wu, Y. Wu, L. Wei, H. Mao, A. Lal, P. Xi, L. Tang, Y. Zhang, Y. Liu, S. Tan and L. Chen, *Nat. Biotechnol.*, 2018, **36**, 451–459.
45 K. D. Malviya, H. Dotan, D. Shlenkevich, A. Tsyganok, H. Mor and A. Rothschild, *J. Mater. Chem. A*, 2016, **4**, 3091–3099.
46 H. Z. Asl and S. M. Rozati, *Appl. Phys. A: Mater. Sci. Process.*, 2019, **125**, 689.
47 A. Kassim, S. Nagalingam, H. S. Min and N. Karrim, *Arabian J. Chem.*, 2010, **3**, 243–249.
48 M. Rydzek, M. Reidinger, M. Arduini-Schuster and J. Manara, *Prog. Org. Coat.*, 2011, **70**, 369–375.
49 A. Helal, J. Yu, A. I. Eid, S. A. El-Hakam, S. E. Samra and S. M. El-Sheikh, *Surf. Interfaces*, 2021, **25**, 101148.
50 L. Palmolahti, J. Hämelahti, M. Hannula, H. Ali-Löytty and M. Valden, *Surf. Coat. Technol.*, 2024, **494**, 131546.
51 R. Khurram, Z. Wang, M. F. Ehsan, S. Peng, M. Shafiq and B. Khan, *RSC Adv.*, 2020, **10**, 44997–45007.
52 P. R. Jubu, F. K. Yam, V. M. Igba and K. P. Beh, *J. Solid State Chem.*, 2020, **290**, 121576.
53 M. R. da Silva, L. H. Dall'Antonia, L. V. A. Scalvi, D. I. dos Santos, L. O. Ruggiero and A. Urbano, *J. Solid State Electrochem.*, 2012, **16**, 3267–3274.
54 M. Chen, X. Chang, Z. Ma, X. Gao and L. Jia, *ACS Appl. Nano Mater.*, 2024, **7**, 15255–15266.
55 Y. Peng, M. Du, X. Zou, G. Jia, S. Permatasari Santoso, X. Peng, W. Niu, M. Yuan and H.-Y. Hsu, *J. Colloid Interface Sci.*, 2022, **608**, 1116–1125.
56 C. Du, X. Yang, M. T. Mayer, H. Hoyt, J. Xie, G. McMahon, G. Bischoping and D. Wang, *Angew. Chem., Int. Ed.*, 2013, **52**, 12692–12695.
57 X. Cao, H. Chen, Z. Lu, Y. Zhao, S. Wei, Y. Liu, J. Zeng, G. Zhang, Q. Ma, L. Zhong, L. Song and Y. Qiu, *J. Colloid Interface Sci.*, 2025, **690**, 137308.
58 J. H. Kim, N. K. Lee, H. W. Kim, Z. Pan and W. Y. Sohn, *J. Photochem. Photobiol., A*, 2023, **437**, 114478.
59 Z. Chen, T. F. Jaramillo, T. G. Deutsch, A. Kleiman-Shwarsctein, A. J. Forman, N. Gaillard, R. Garland, K. Takanabe, C. Heske, M. Sunkara, E. W. McFarland, K. Domen, E. L. Miller, J. A. Turner and H. N. Dinh, *J. Mater. Res.*, 2010, **25**, 3–16.
60 B. Iandolo, H. Zhang, B. Wickman, I. Zorić, G. Conibeer and A. Hellman, *RSC Adv.*, 2015, **5**, 61021–61030.
61 R. G. M. Oliveira, J. E. V. de Morais, G. S. Batista, M. A. S. Silva, J. C. Goes and A. S. B. Sombra, *J. Alloys Compd.*, 2019, **775**, 889–895.
62 T. Chugenji, Z. Pan and K. Katayama, *J. Phys. Chem. C*, 2022, **126**, 19319–19326.
63 N. K. Lee and W. Y. Sohn, *ChemPhotoChem*, 2024, **8**, e202300301.
64 J. H. Kim, J. M. Kim, Z. Pan and W. Y. Sohn, *J. Photochem. Photobiol., A*, 2023, **445**, 115037.
65 F. Le Formal, S. R. Pendlebury, M. Cornuz, S. D. Tilley, M. Grätzel and J. R. Durrant, *J. Am. Chem. Soc.*, 2014, **136**, 2564–2574.
66 M. Barroso, S. R. Pendlebury, A. J. Cowan and J. R. Durrant, *Chem. Sci.*, 2013, **4**, 2724–2734.
67 M. Barroso, A. J. Cowan, S. R. Pendlebury, M. Grätzel, D. R. Klug and J. R. Durrant, *J. Am. Chem. Soc.*, 2011, **133**, 14868–14871.
68 A. Minato, K. Katayama and W. Y. Sohn, *J. Photochem. Photobiol., A*, 2022, **424**, 113659.
69 J. Tang, X. Zhong, G. Zhou, W. Chen, T. Wu and F. Sun, *J. Alloys Compd.*, 2025, **1032**, 181067.
70 J. P. Deebasree, V. Maheskumar and B. Vidhya, *Ultrason. Sonochem.*, 2018, **45**, 123–132.
71 M. Li, L. Zhao and L. Guo, *Int. J. Hydrogen Energy*, 2010, **35**, 7127–7133.